LANGMUIR

pubs.acs.org/Langmuir Article

Strengthened Built-In Electric Field in Sulfur-Doped BiOBr Facilitates Exciton Dissociation and Boosts Photocatalytic Activity

Lingzhi Shen, Zhenchao Li, Daguang Li,* Chenghui Wen, Zheng Fang, Zili Lin, Wenjun Li, Jiaxing Huang, Ningyu Tu, Wenying Lv,* and Guoguang Liu

Cite This: *Langmuir* 2026, 42, 8006–8017 Read Online

ACCESS | Metrics & More | Article Recommendations | Supporting Information

ABSTRACT: The effective promotion of exciton dissociation to increase the electron density in BiOBr has garnered significant attention. Here, we effectively promote exciton dissociation and enhance photocatalytic activity through a simple sulfur-doped strategy. We demonstrated that sulfur doping markedly increased the built-in electric field (BIEF) strength of BiOBr, which in turn provided the driving force for exciton dissociation and promoted the rapid separation and transport of charge carriers. Additionally, the introduction of abundant oxygen vacancies on BiOBr enhanced its ability to activate oxygen. Consequently, in degradation experiments, S-doped BiOBr exhibited an 8.07-fold increase in the degradation rate of sulfisoxazole (SIZ) compared to that of pure BiOBr. Following this, quenching experiments and electron spin resonance identified holes, superoxide, and singlet oxygen as the primary reactive species involved in photocatalysis, leading to the proposal of a photocatalytic mechanism. Furthermore, liquid chromatography–mass spectrometry identified 8 intermediate products and elucidated three degradation pathways. Finally, the impact of different influencing conditions on the degradation of the SIZ was thoroughly examined. To summarize, this study proposes a strategy to enhance photocatalytic activity by adjusting the BIEF and manipulating exciton effects, providing a new perspective on charge transfer mechanisms in photocatalytic systems.

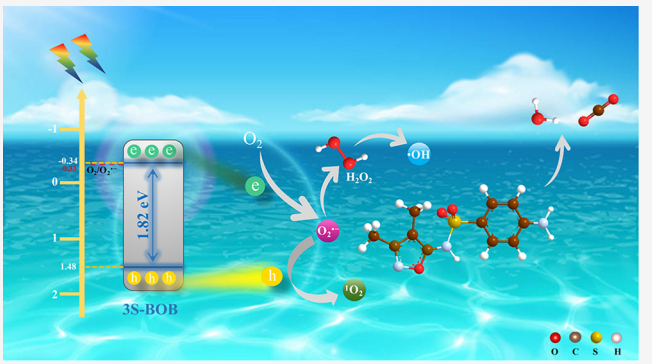

INTRODUCTION

As a typical emerging contaminant, the sulfonamide antibiotic sulfisoxazole (SIZ) exhibits considerable environmental persistence and mobility in water bodies.[1−4] Its presence poses dual threats of direct ecotoxicity and the long-term selection pressure for antimicrobial resistance.[5−7] Furthermore, SIZ has been classified as a possible human carcinogen, elevating public health concerns regarding its environmental dissemination.[8] These combined risks highlight the critical need for advanced remediation strategies capable of its effective degradation.

In recent years, solar semiconductor photocatalysis has gained widespread attention due to its high efficiency, environmental friendliness, strong adaptability, and low secondary pollutant formation.[9,10] Among these, BiOBr has received extensive research attention in environmental remediation due to its unique bandgap structure, appropriate bandgap energy, good optical stability, and effective oxidation capability.[11,12] Conventional perspectives on the photocatalytic mechanism of BiOBr have mainly emphasized charge carrier separation. However, these commonly accepted views often neglect the presence of excitonic effects.[13] For instance, Wang et al. elucidated the excitonic properties of BiOBr materials exhibiting a layered structure.[14] Introducing the concept of excitons reveals that our traditional understanding of photocatalysis becomes incomplete. Excitons are neutral singlet states formed when electron–hole pairs cannot fully separate due to the Coulombic interaction within the material during photoexcitation.[15] In photocatalytic reactions dominated by charge carriers, the competitive relationship between excitons and charge carriers severely limits the formation of free charges, resulting in significantly reduced photocatalytic efficiency.[16,17] Therefore, it is crucial to effectively promote exciton dissociation in materials through reasonable modification methods to achieve a substantial yield of charge carriers.

Previous studies have shown that introducing energy disorder in catalysts is a viable strategy to promote exciton dissociation and reduce exciton stability.[18,19] For instance, Shi et al. induced band offset arrangements by surface doping with P, disrupting exciton stability;[20] Wang et al. and Wu et al.

Received: December 25, 2025
Revised: March 4, 2026
Accepted: March 5, 2026
Published: March 13, 2026

promoted exciton dissociation through defect engineering by introducing oxygen vacancies, disrupting the balance of band edge states around defect sites.[21,22] Zhou et al. also weakened exciton effects by constructing heterojunctions.[13] Recently, studies have also found that built-in electric fields (BIEF) can provide driving forces for exciton dissociation, thereby facilitating the separation of electron−hole pairs.[23−25] To the best of our knowledge, few studies have integrated built-in electric fields and excitonic effects in BiOBr research. Fortunately, the symbiotic crystal structure of $[Bi_2O_2]^{2+}$ and $[Br_2]^{2-}$ layers in BiOBr induces a nonuniform charge distribution, which is expected to successfully construct built-in electric fields and improve carrier separation and migration.[26] Additionally, nonmetal doping has been reported to regulate the strength of built-in electric fields.[27] This is primarily because the introduced dopant atoms, possessing different electronegativity and atomic radii compared to the host atoms, can distort the local electronic structure and create charge imbalance, thereby modulating the intrinsic polarization and the associated BIEF. Motivated by these insights, we present a simple approach here: inserting sulfur between BiOBr layers to induce polarization and adjust the strength of the built-in electric field, thereby providing driving forces for exciton dissociation.

Therefore, the present work aims to precisely modulate the BIEF of BiOBr via a facile sulfur-doping strategy, thereby facilitating exciton dissociation and enhancing the photocatalytic efficiency. A series of sulfur-doped BiOBr (xS-BOB) samples were synthesized and systematically characterized to unravel the correlations among S-doping, BIEF enhancement, oxygen vacancy formation, and charge carrier dynamics. The photocatalytic performance was evaluated by degrading SIZ under blue light with the degradation pathways and intermediates elucidated. Furthermore, the effects of key environmental parameters on the degradation process were investigated to assess the practical applicability. This study provides a new perspective on charge transfer mechanisms in photocatalytic systems. More importantly, this work establishes a quantitative structure−activity relationship among anionic doping, BIEF, and exciton dissociation efficiency in layered BiOBr, offering a generalizable design principle for exciton management in analogous photocatalysts.

EXPERIMENTAL SECTION

Chemical Reagents

Details of the reagents and ultrapure water used in this experiment are provided in Text S1.

Synthesis

The fabrication of S-doped BiOBr followed a previously reported method with some modifications.[23] During the preparation, 4 mmol of $Bi(NO_3)_3{\cdot}5H_2O$ was added to 50 mL of ethylene glycol, followed by the addition of 4 mmol of KCl. After mixing for 60 min, different amounts of thiourea (2, 3, 4, 5 mmol) were added as the sulfur source, followed by vigorous stirring for another 30 min. Subsequently, the mixture was transferred to a Teflon-lined autoclave and maintained at 160 °C for 12 h. Following cooling, the product was retrieved via centrifugation, subjected to multiple washes with ultrapure water and ethanol, and then dried in an oven at 60 °C. The collected products were labeled as xS-BOB (x = 2, 3, 4, 5) according to the amount of thiourea added. The preparation process for pure BiOBr was the same but without the addition of thiourea.

Characterization

Detailed information on characterization is provided in Text S2.

Photocatalytic Activity Tests

All experiments were conducted by using low-power blue LED lamps (9W, 455 nm) for degradation experiments. The reactor utilized a vertical top-irradiation configuration with the light source positioned 5 cm directly above the suspension surface. The reaction temperature was maintained at 25 °C using a thermostatic magnetic stirrer (Figure S1). Initially, the prepared catalyst (20 mg) was suspended in 50 mL of a 10 mg L^{-1} SIZ aqueous solution and stirred in darkness for 30 min to reach adsorption−desorption equilibrium. Subsequently, during illumination, 1 mL of the suspension was intermittently filtered using a 0.22 μm filter and subjected to analysis via high-performance liquid chromatography (HPLC). The detailed chromatographic conditions and instrument parameters are provided in Text S3 and Table S1.

Theoretical Calculations

All calculations were performed within the framework of spin-polarized density functional theory (DFT) using the Vienna Ab initio Simulation Package (VASP) with the projector augmented wave (PAW) method. The methods and details of theoretical calculations are provided in Text S4.

RESULTS AND DISCUSSION

Morphology and Structure

The prepared samples underwent characterization via SEM. Figure 1a shows that the original BiOBr consisted of

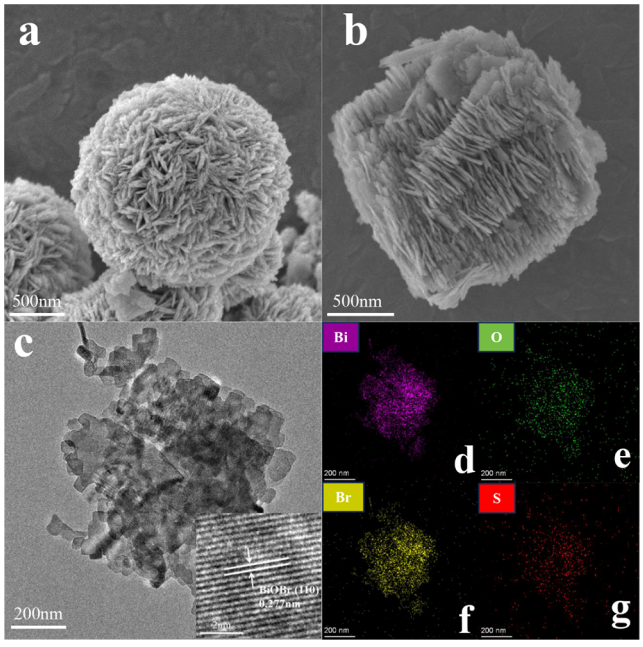

Figure 1. SEM images of (a) BiOBr and (b) 3S-BOB; (c) TEM images of 3S-BOB; (d−g) STEM elemental mapping of the 3S-BOB composite.

microspheres assembled from densely packed nanosheets. Upon the introduction of sulfur, the morphology of 3S-BOB changed (Figure 1b), with the stacked nanosheets forming a rectangular structure instead of microspheres. This change might have been due to the strong interactions between S^{2-} and Bi^{3+} affecting the stacking of the positively charged $[Bi_2O_2]$ layers and the doubly negatively charged $[Br_2]^{2-}$ layers.[28] Figure 1c shows TEM images of 3S-BOB, revealing a rectangular structure formed by stacked nanosheets, consistent with the SEM observations. The HRTEM image (Figure 1c inset) revealed that 3S-BOB possessed a distinct

https://doi.org/10.1021/acs.langmuir.5c06805
Langmuir 2026, 42, 8006−8017

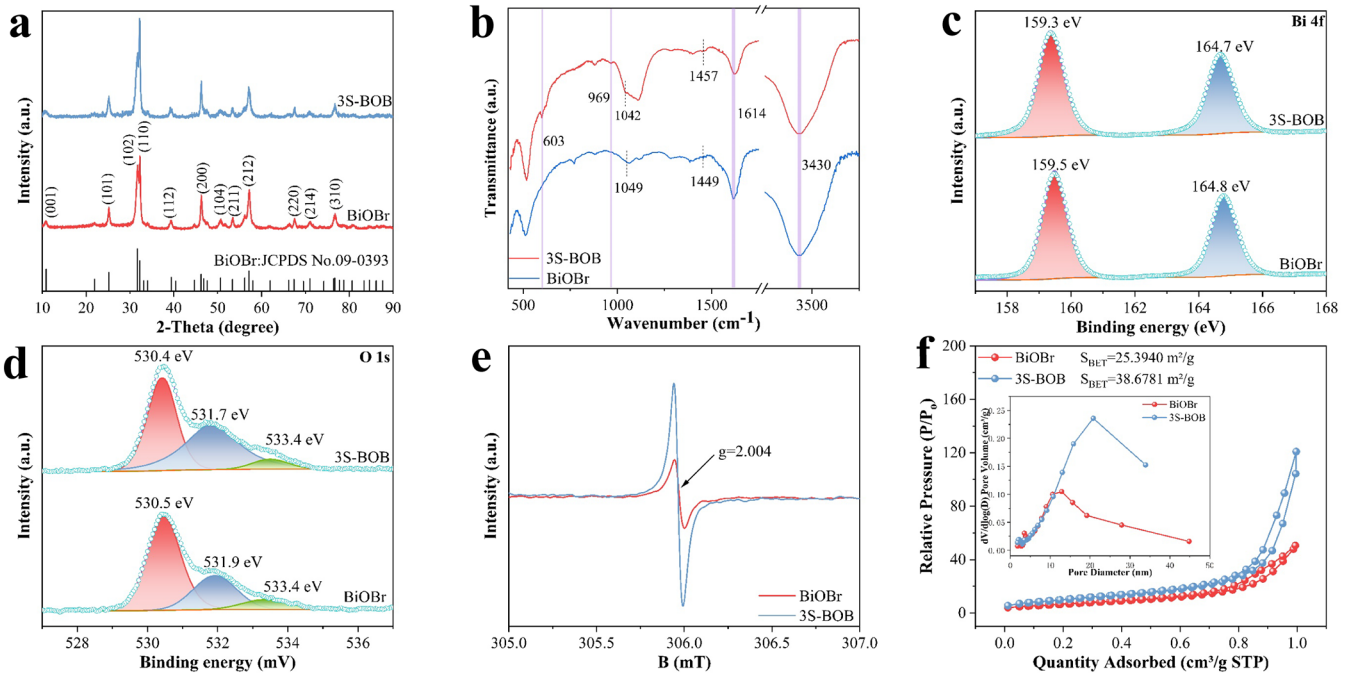

Figure 2. (a) XRD pattern and (b) FT-IR spectra of the as-prepared samples. XPS spectra of (c) Bi 4f, (d) O 1s, (e) EPR spectra, and (f) N_2 adsorption−desorption isotherms and the pore size distribution (illustration) of BiOBr and 3S-BOB.

lattice spacing of 0.277 nm, which could be assigned to the (110) plane of BiOBr. Elemental mapping indicated that Bi, O, Br, and S were uniformly distributed in the sample, confirming the successful doping of S into the BiOBr structure (Figure 1d−g).

The phase structures of BiOBr and 3S-BOB were analyzed using XRD. As shown in Figure 2a, the (001), (101), (102), (110), (112), (200), and (212) crystal planes of both samples were accurately attributed to the characteristic peaks of BiOBr at 10.9°, 25.1°, 31.7°, 32.2°, 39.4°, 46.2°, and 57.1°, which were consistent with the standard diffraction pattern of BiOBr (JCPDS Card No. 09-0393). With the doping of S, no impurity peaks were detected, indicating that a small amount of S doping did not cause a phase transformation in BiOBr nanocrystals. Additionally, the intensity of the characteristic peaks of 3S-BOB increased, suggesting that S doping resulted in well-ordered and enhanced growth of BiOBr crystal planes.[29]

The functional groups of BiOBr and 3S-BOB were investigated by using Fourier-transform infrared spectroscopy (FT-IR). As shown in Figure 2b, the FT-IR spectrum of 3S-BOB displayed additional peaks at 603 and 969 cm^{-1}, which can be ascribed to the vibrations of Bi−S bonds.[30,31] This finding confirmed the strong bonding between the doped S atoms and Bi. Additionally, the peaks of Bi−Br in BiOBr at 1049 and 1449 cm^{-1} shifted to 1042 and 1457 cm^{-1}, respectively, indicating that Br elements in the interlayers may have been replaced by S elements.[28,32] Finally, the peaks observed at 3430 and 1614 cm^{-1} were associated with the stretching and bending vibrations of adsorbed H_2O molecules,[33] respectively.

The chemical structure changes of the samples were further investigated by using XPS analysis. From Figure S2a, it was observed that the Br 3d peaks shifted from 68.5 and 69.5 eV to 68.4 and 69.4 eV, indicating that Br^- had been replaced by S^{2-} through anion exchange due to the weakened van der Waals forces between $[Br_2]^{2-}$ layers.[28] The Bi 4f peaks corresponding to Bi $4f_{7/2}$ and Bi $4f_{5/2}$ appeared at 159.3 and 164.7 eV, respectively, with a decrease in binding energy of 0.2 and 0.1 eV (Figure 2c). This indicated that the introduction of S altered the chemical environment of Bi atoms, which is consistent with the formation of Bi−S bonds.[23,34] It is worth noting that the S 2p peaks significantly overlapped with the Bi 4f orbitals, making it challenging to distinguish S elements based on S 2p XPS results. However, the detection of additional S 2s peaks at binding energies of 225.6 and 228.2 eV (Figure S2b) confirmed the incorporation of S into the BiOBr crystal structure.[35,36] In addition to the surface elemental analysis, the bulk sulfur content of the xS-BOB samples was measured to be consistent with the stoichiometric ratios (Table S2), further supporting the successful incorporation of sulfur. The O 1s XPS spectrum of 3S-BOB (Figure 2d) exhibited peaks at 530.4, 531.7, and 533.4 eV, corresponding to lattice oxygen, oxygen vacancies (OVs), and surface hydroxyl groups.[37] The proportion of OVs in 3S-BOB significantly increased from 27% to 45%, indicating that the introduction of sulfur induced the formation of numerous OVs, thereby facilitating the activation of O_2.[1]

The formation of OVs in BiOBr and 3S-BOB was further detected by EPR spectroscopy. Figure 2e showed that both samples had typical EPR signals centered at g = 2.004, which were determined to be oxygen vacancies capturing electrons.[38] The signal intensity of 3S-BOB was significantly higher than that of pure BiOBr, indicating a higher concentration of oxygen vacancies in 3S-BOB.

The specific surface area and pore structure of the samples were characterized by using nitrogen adsorption−desorption isotherms. As depicted in Figure 2f, both samples displayed typical type IV isotherms with pronounced hysteresis loops, indicating the presence of mesopores.[39] The specific surface areas of BiOBr and 3S-BOB were 25.39 and 38.67 $m^2\ g^{-1}$, respectively. Additionally, pore size distribution data indicated

https://doi.org/10.1021/acs.langmuir.5c06805
Langmuir 2026, 42, 8006−8017

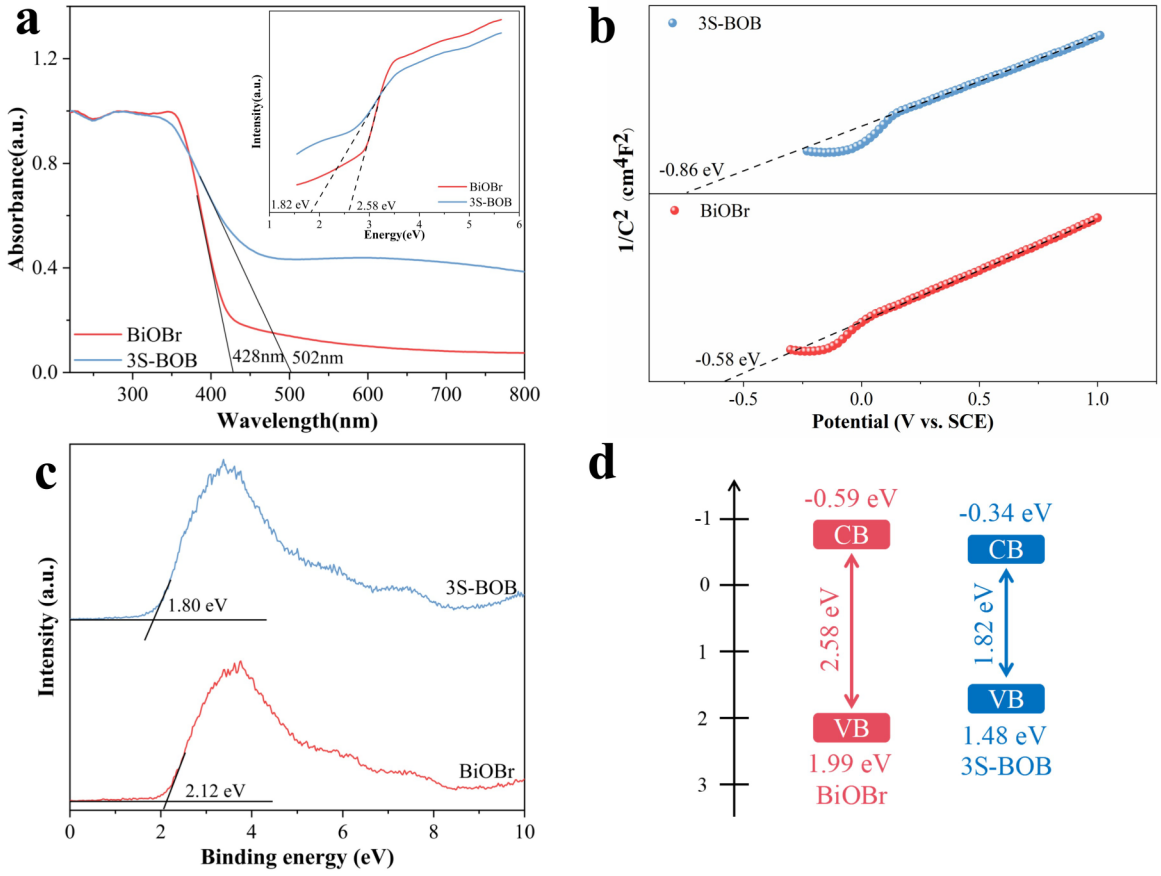

Figure 3. (a) UV−vis diffuse reflectance spectra and Tauc's plot (illustrations), (b) Mott−Schottky plot, (c) VB-XPS valence band analysis, and (d) schematic band structure evolution of BiOBr and 3S-BOB.

that compared to BiOBr's pore volume (0.078 $cm^3\ g^{-1}$) and average pore diameter (12.31 nm), 3S-BOB exhibited a larger pore volume (0.189 $cm^3\ g^{-1}$) and average pore diameter (19.34 nm). This could have provided more catalytically active sites, thereby enhancing photocatalytic activity.

Photophysical Properties

The optical absorption characteristics of 3S-BOB were comprehensively studied using a UV−vis diffuse reflection test. As shown in Figure 3a, the introduction of sulfur into 3S-BOB significantly enhanced its optical absorption range, shifting from 428 to 502 nm. The band gap (E_g) of BiOBr and 3S-BOB decreased significantly from 2.58 to 1.82 eV. It is important to note that while a narrower band gap can, in principle, also accelerate charge recombination, the overall photocatalytic efficacy is determined by the net balance between carrier generation and separation. As will be elucidated in the following sections, the key to the enhanced performance of 3S-BOB lies not only in its improved light absorption but, more critically, in its superior ability to separate and utilize these photogenerated charges.[40] Furthermore, to elucidate the flat band potentials (E_{fb}) and band structures of BiOBr and 3S-BOB, Mott−Schottky tests were conducted. In Figure 3b, the positive slope of the extrapolated line indicates that both BiOBr and 3S-BOB are n-type semiconductors.[41] Subsequently, the E_{fb} of BiOBr and 3S-BOB were −0.58 eV and −0.86 eV vs SCE (−0.13 eV and −0.32 eV vs NHE), respectively. Due to the equivalence of the E_{fb} of n-type semiconductors with the Fermi level, the relative Fermi levels of BiOBr and 3S-BOB were −0.13 eV and −0.32 eV versus NHE.[42] Based on the VB-XPS data, it was established with confidence that the band gaps separating the Fermi level from the VB were 2.12 and 1.80 eV for both BiOBr and 3S-BOB, respectively (Figure 3c). Therefore, the calculated VB positions of BiOBr and 3S-BOB were 1.99 and 1.48 eV versus NHE. Based on the formula: $E_{CB} = E_{VB} - E_g$, the CB positions relative to NHE for BiOBr and 3S-BOB were determined to be −0.59 eV and −0.34 eV, respectively,[15] as displayed in Figure 3d.

The Intensified BIEF Field Facilitates Exciton Dissociation

Efficient separation and transport of photogenerated charge carriers significantly influence the efficacy of photocatalysts.[43] As a driving force, a strong BIEF facilitates exciton dissociation, promoting effective charge separation and rapid transport of photogenerated charges.[44,45] On the other hand, the insertion of S ions causes a nonuniform distribution of interlayer charges in BiOBr, facilitating adjustment of BIEF.[46] For estimation of the BIEF in our samples, we utilized the model proposed by Kanata et al.[47] According to this model, the strength of BIEF and the surface potential varied in direct proportion to the square root of the surface charge density product (Text S5). Surface potential measurements were conducted using Kelvin probe force microscopy (KPFM), where the surface charge density correlated to the zeta potential. Figure 4a−c illustrates that the surface potential of 3S-BOB (ΔE = 29.2 mV) exceeded that of BiOBr (ΔE = 20.1 mV). Furthermore, the zeta potential of 3S-BOB (−34.9 mV) was 2.3 times larger than that of BiOBr (−15.4 mV). These results demonstrated that sulfur doping effectively enhanced BIEF.

https://doi.org/10.1021/acs.langmuir.5c06805
Langmuir 2026, 42, 8006−8017

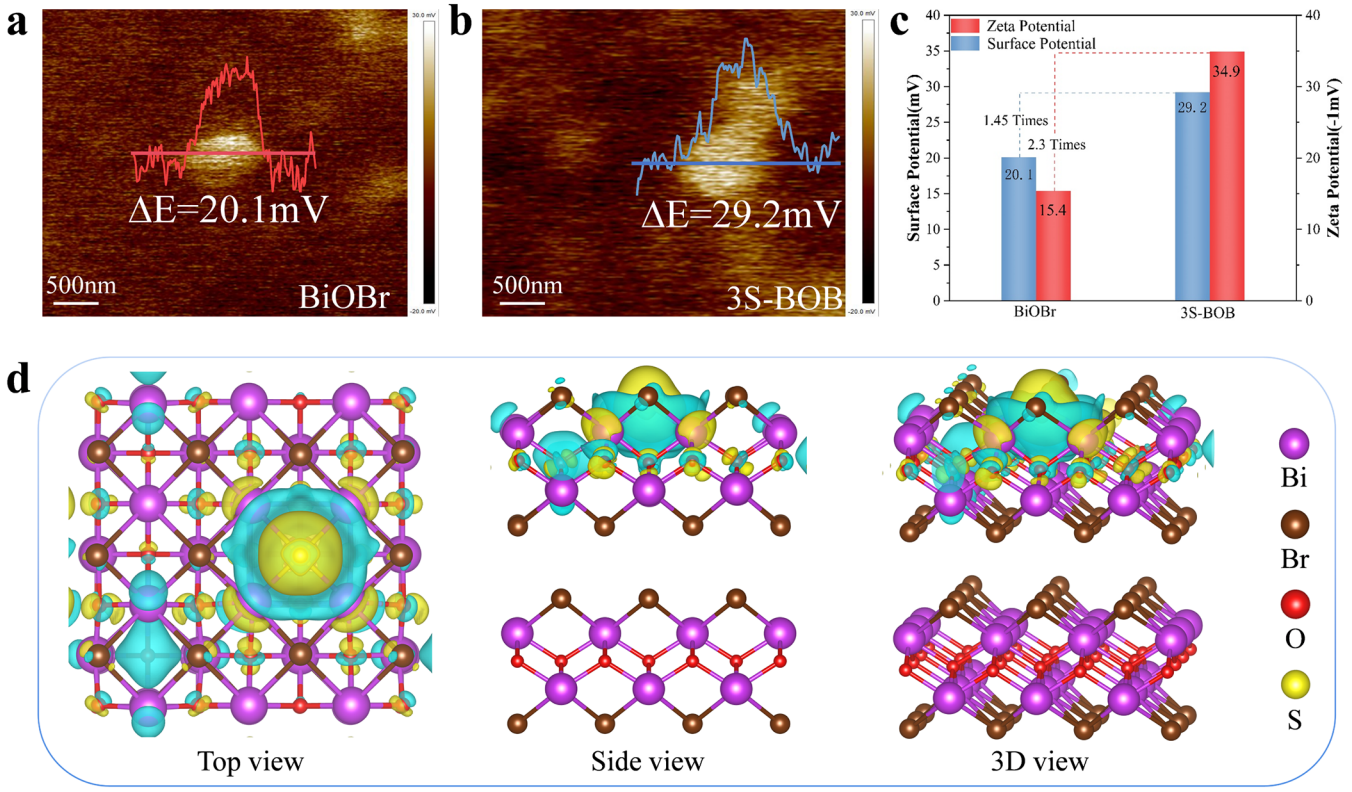

Figure 4. Surface potential of (a) BiOBr and (b) 3S-BOB detected with KPFM, (c) zeta potential and surface potential of BiOBr and 3S-BOB, and (d) differential charge density graphic of 3S-BOB (cyan and yellow colors represent electron depletion and electron accumulation regions, respectively).

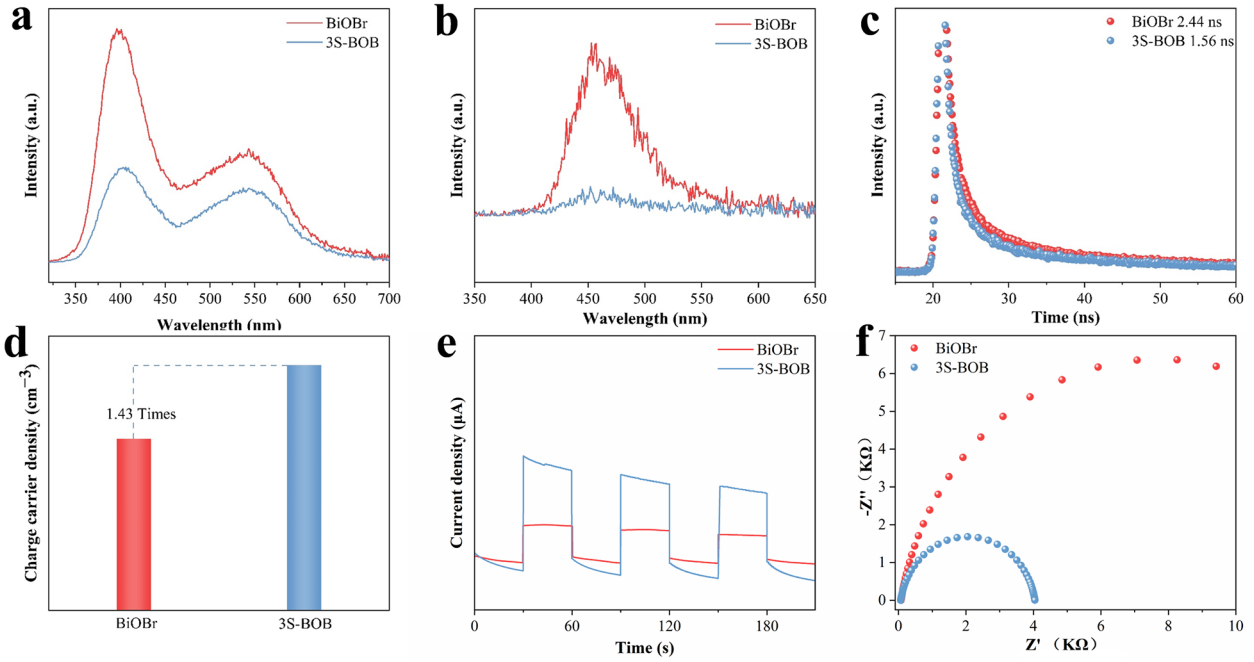

Figure 5. (a) Photoluminescence (PL) spectra, (b) phosphorescence (PH) spectra, (c) time-resolved photoluminescence (TRPL) decay spectra, (d) electron concentration ratio, (e) transient photocurrent, and (f) electrochemical impedance spectroscopy (EIS) spectra of BiOBr and 3S-BOB.

To explore the photoinduced electron transition mechanism of 3S-BOB, first-principles calculations based on density functional theory (DFT) were performed. The geometric structural model of S-doped BiOBr with oxygen vacancies is presented in Figure S3. As shown in Figure 4d, S atoms with lower electronegativity replaced Br atoms, forming a high charge density in the sulfur-doped layer. The strong Bi−S bond contributed to electron depletion at the Bi atom sites (cyan region) and electron accumulation at the S atom sites (yellow region), thereby generating strong interlayer polar-

https://doi.org/10.1021/acs.langmuir.5c06805
Langmuir 2026, 42, 8006−8017

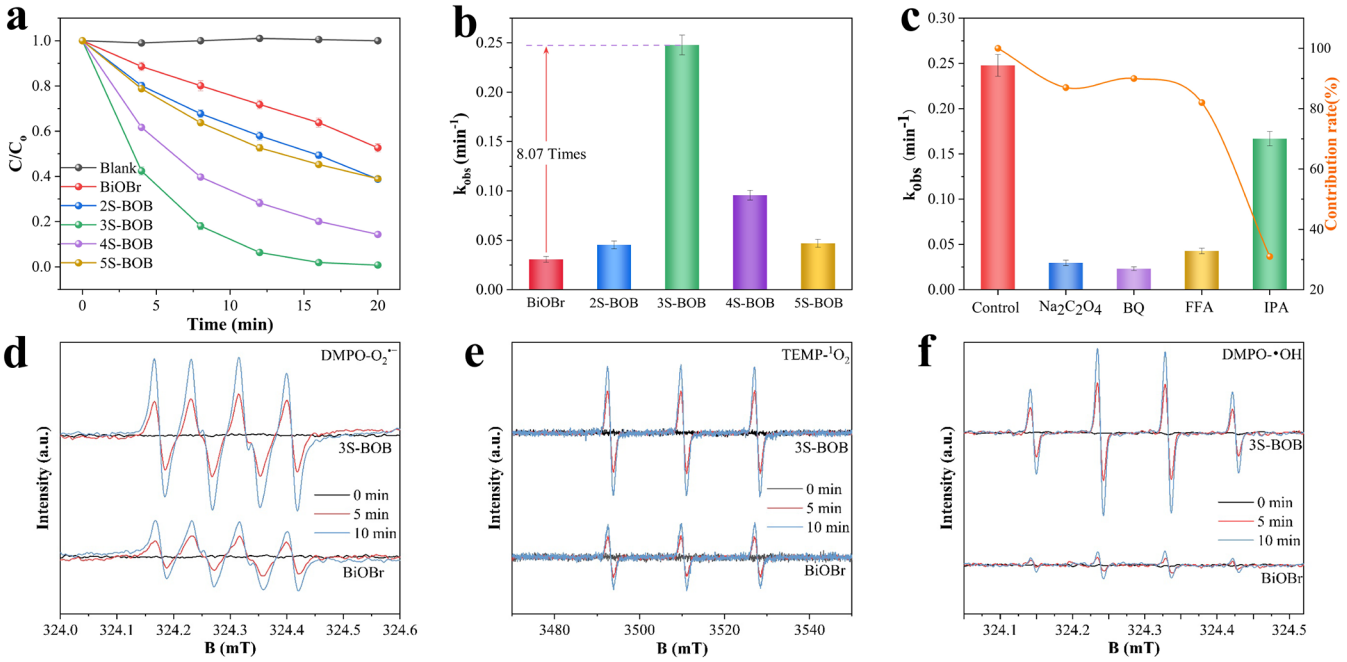

Figure 6. (a) Performance activities, (b) pseudo-first-order rate constant, (c) rate constants, and inhibition effects of SIZ photodegradation in the presence of various scavengers. EPR spectra of (d) DMPO-$O_2^{\bullet-}$, (e) TEMP-$^1O_2$, and (f) DMPO-•OH of the BiOBr and 3S-BOB.

ization. Generally, polarization can enhance the BIEF, acting as the driving force for carrier separation and transport.[48] Additionally, electron depletion occurs in oxygen vacancy regions, making them prone to attracting photogenerated electrons and potentially promoting exciton dissociation.

To clearly elucidate the excitonic processes in the S-doped BiOBr photocatalytic system, we employed photoluminescence (PL) spectroscopy. Figure 5a displays the steady-state PL spectra, acknowledged as a robust approach for investigating exciton dissociation. Excitons generally relaxed to the ground state by radiating photons, so the detected fluorescence was formed by the decay of singlet excitons as observed.[18,49] Compared to BiOBr, the PL signal intensity of 3S-BOB significantly decreases, indicating a reduced concentration of singlet excitons.

Typically, the reduction in singlet excitons transitions into triplet excitons or dissociates into free charges within the system. Therefore, steady-state phosphorescence (PH) spectra provide additional insights, as the PH signal originates from the decay of triplet excitons.[13,14] From Figure 5b, it was evident that both samples exhibited signals of triplet excitons, with 3S-BOB showing a significantly reduced PH signal compared to BiOBr. This indicated a lower yield of triplet excitons in 3S-BOB, suggesting that the dissociation of singlet excitons into electron holes was the primary reason for the decrease in singlet exciton concentration.

As shown in Figure 5c, we utilized time-resolved fluorescence decay spectroscopy to analyze the lifetime of singlet excitons.[50] Using the formula (Text S6), we calculated the exciton lifetimes of BiOBr and 3S-BOB as 2.44 and 1.56 ns, respectively. Compared to BiOBr, 3S-BOB exhibited a shorter lifetime of singlet excitons, indicating a significantly enhanced efficiency in singlet exciton dissociation.[51] This suggested that tuning the built-in electric field through sulfur doping effectively promoted the efficiency of exciton dissociation, thereby facilitating the generation of more free charges.

According to the Mott−Schottky equation, the slope is inversely proportional to the electron concentration, allowing us to estimate the electron concentration in the samples.[52] By using the formula (Text S7), we calculated that the electron concentration in 3S-BOB was 1.43 times higher than that in BiOBr (Figure 5d). Additionally, from the transient photocurrent response (Figure 5e), it was evident that 3S-BOB exhibited notably elevated photocurrent density, signifying effective dissociation of excitons into free charges and a rise in electron concentration.[53] Furthermore, from the electrochemical impedance spectroscopy (EIS) plot (Figure 5f), 3S-BOB showed a smaller radius, indicating lower impedance encountered during electron transfer.[54] This underscored that an enhanced built-in electric field reduced transport resistance, thereby improving charge migration capability.

Photocatalytic Degradation Performance and Mechanism

This research investigated the photodegradation capabilities of the synthesized compounds, with an emphasis on SIZ, a commonly prescribed antibiotic. As shown in Figures S4 and S7, prior to conducting photocatalytic experiments, the prepared samples were preliminarily studied for their adsorption of SIZ. All samples reached adsorption−desorption equilibrium within 30 min. BiOBr exhibited the lowest adsorption capacity for SIZ, whereas 3S-BOB showed the highest, consistent with the BET results. Subsequently, under blue light irradiation, SIZ was completely degraded by 3S-BOB samples in just 20 min (Figure 6a). In contrast, pure BiOBr exhibited lower degradation efficiency, removing only 50% of SIZ in the same time frame. The kinetic rate constants (k_{obs}) were calculated using pseudo-first-order kinetics (Figure 6b), with 3S-BOB's k_{obs} (0.2478 min^{-1}) showing an approximately 8.07-fold increase compared to BiOBr's (0.0307 min^{-1}). Clearly, among all of the prepared samples, 3S-BOB demonstrated superior photocatalytic activity for SIZ degradation.

https://doi.org/10.1021/acs.langmuir.5c06805
Langmuir 2026, 42, 8006−8017

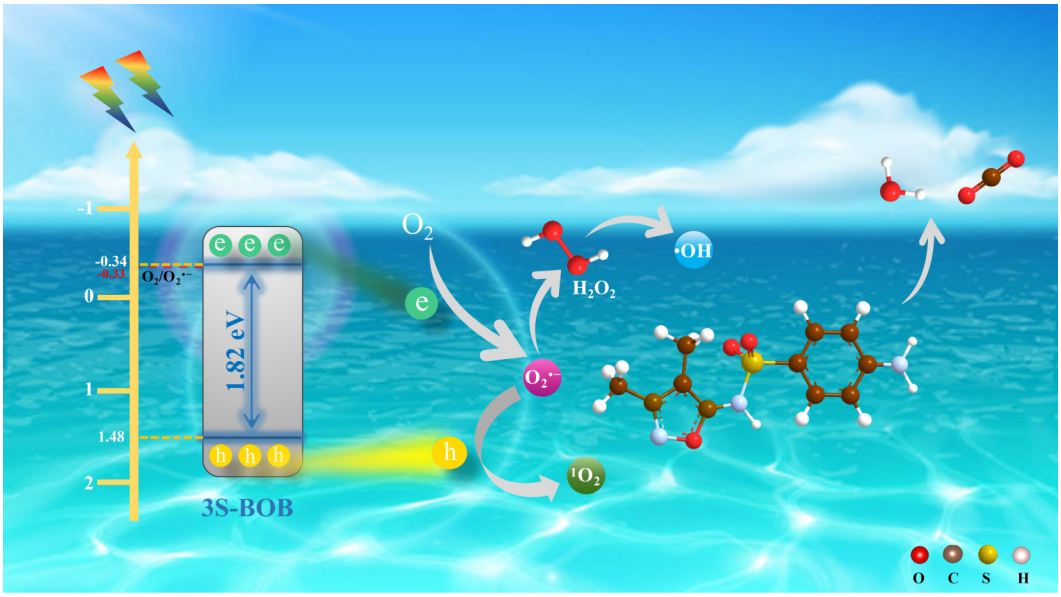

Figure 7. Illustration of the potential photocatalytic mechanism of the 3S-BOB.

Additional cycling tests were conducted under blue light irradiation to investigate the stability of the composite material. After four cycles (Figure S5a), 3S-BOB maintained a degradation efficiency of over 80% and preserved high catalytic performance. This result demonstrates the satisfactory reusability of the photocatalyst. Furthermore, XRD and FT-IR analyses (Figure S5b,c) confirmed that the crystal structure of 3S-BOB remained unchanged after four cycles, indicating its remarkable stability and recyclability. However, a slight decline in activity was still observable over the four cycles. This may be attributed to the following factors: (1) Partial loss of active components: Minimal leaching of the doped S species or Bi^{3+} ions might occur during the cyclic reactions, as suggested by the slight attenuation of the Bi−S bond vibration peak in the postcycling FT-IR spectrum (Figure S5c). (2) Surface passivation: The adsorption and accumulation of intermediate organic fragments or inorganic ions (from the reaction matrix) on the catalyst surface could partially block the active sites and hinder light absorption.[55]

To investigate the contribution of various reactive species (RSs) in the 3S-BOB photocatalytic system, we conducted quenching experiments (details in Text S9). Initially, we used 10 mM sodium oxalate, *p*-benzoquinone, furfuryl alcohol, and IPA to quench holes, superoxide radicals, singlet oxygen, and hydroxyl radicals, respectively. As shown in Figure 6c, after 20 min of illumination, the reaction rate constants of 3S-BOB for sodium oxalate, *p*-benzoquinone, furfuryl alcohol, and IPA were 0.0329, 0.0161, 0.0424, and 0.2195 min^{-1}, respectively. Thus, the photodegradation contribution rates of h^+, $O_2^{\bullet-}$, $^1O_2$, and •OH were 91.45%, 95.75%, 88.95%, and 43.42%, respectively. This indicated that h^+, $O_2^{\bullet-}$, and $^1O_2$ played crucial roles in the degradation process.

To further confirm the reactive species (RSs), an electron spin resonance (ESR) technique is commonly employed to determine their generation during photocatalysis. We used DMPO to capture superoxide and hydroxyl radicals formed during the photocatalytic process and TEMP to capture singlet oxygen. As shown in Figure 6d,e, both samples exhibited characteristic ESR signals corresponding to the DMPO-$O_2^{\bullet-}$, TEMP-$^1O_2$, and DMPO-•OH adducts, confirming the formation of $O_2^{\bullet-}$, $^1O_2$, and •OH during photocatalysis. Moreover, compared to BiOBr, the ESR signal of 3S-BOB was significantly enhanced, clearly demonstrating that sulfur doping induced oxygen vacancies and increased BIEF, significantly promoting thermally electron-mediated RSs in the 3S-BOB system.

Due to the enhanced ability of 3S-BOB to activate molecular oxygen, we quantified the concentration of superoxide using the NBT assay (Text S10) to evaluate its activation capability.[56] As observed in Figure S6a,b, the NBT concentration steadily decreased with prolonged radiation. Calculations showed that the concentration of $O_2^{\bullet-}$ generated was 1.065×10^{-5} M and 3.068×10^{-5} M for BiOBr and 3S-BOB, respectively, indicating a 2.9-fold increase by 3S-BOB compared to BiOBr. Additionally, degradation experiments under different atmospheres were conducted. As shown in Figure S6c, the degradation rate of 3S-BOB was significantly reduced under a N_2 atmosphere, while the adsorption of SIZ in an O_2-saturated solution remained consistent with the normal results (Figure S6d). This confirms the crucial role of O_2 in the conversion of reactive species (RSs).[57] These results indicated that 3S-BOB possessed an excellent molecular oxygen activation capability.

Based on our aforementioned research, we proposed a plausible photocatalytic degradation mechanism for 3S-BOB (Figure 7). Under illumination, photogenerated charge carriers were generated on the surface of 3S-BOB, with electrons excited to the CB and holes remaining in the VB. However, due to Coulombic interactions within the material, they readily entangled to form excitons. Fortunately, the enhanced BIEF reduced the binding energy of excitons, promoting their dissociation into free charges. Subsequently, photoexcited electrons can react with O_2 to generate $O_2^{\bullet-}$, as the CB potential is more negative than the reduction potential E (O_2/$O_2^{\bullet-}$; −0.33 eV). Electrons activated molecular oxygen generation via a charge transfer process, where some superoxide subsequently transformed into $^1O_2$ or •OH. These reactive species then attacked the active sites of sulfonamide molecules, leading to bond cleavage and effective pollutant elimination (eqs 16). Therefore, a synergistic

https://doi.org/10.1021/acs.langmuir.5c06805
Langmuir 2026, 42, 8006−8017

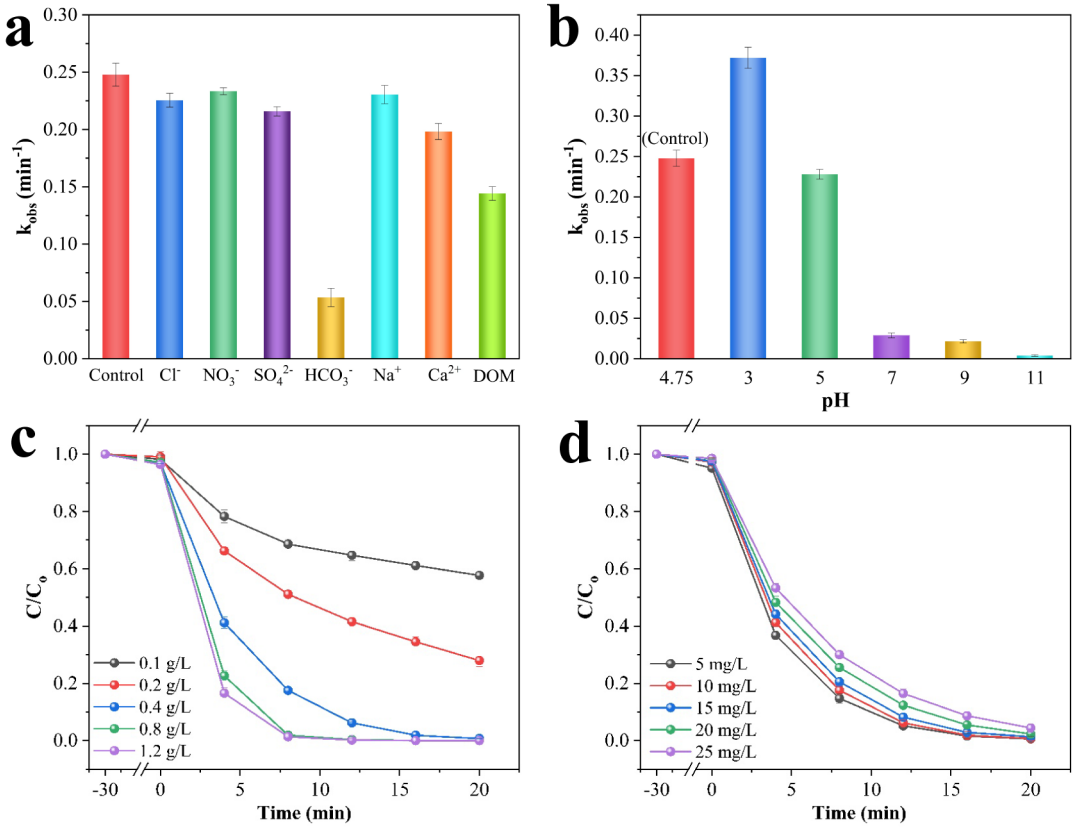

Figure 8. Effect of (a) different ions at a concentration of 10 mM, (b) initial pH change, (c) different catalyst additions, and (d) different SIZ additions on the degradation of SIZ by 3S-BOB.

relationship is established between the strengthened BIEF and the abundant OVs in the 3S-BOB system. The BIEF primarily acts as the driving force to dissociate excitons and accelerate the migration of electrons to the surface, while the OVs function as key active sites to capture these migrating electrons and facilitate the activation of molecular oxygen. This efficient coupling significantly suppresses charge recombination and ensures the maximum utilization of photogenerated carriers for the degradation process.

$$3S\text{-}BOB + hv \rightarrow h^+ + e^- \quad (1)$$

$$O_2 + e^- \rightarrow O_2^{\bullet -} \quad (2)$$

$$O_2^{\bullet -} + h^+ \rightarrow {}^1O_2 \quad (3)$$

$$O_2^{\bullet -} + e^- + 2H^+ \rightarrow H_2O_2 \quad (4)$$

$$H_2O_2 + e^- \rightarrow \bullet OH + OH^- \quad (5)$$

$$({}^1O_2, O_2^{\bullet -}, \bullet OH, h^+) + SIZ \rightarrow Products \quad (6)$$

Effect of Different Factors on Degradation

To investigate the interference of different factors in the 3S-BOB photocatalytic system, we studied the effect of major cations and anions on degradation. Figure 8a shows the influence of common ions in water on the 3S-BOB system. In the presence of Cl^-, NO_3^-, SO_4^{2-}, and Na^+, the catalytic system showed a minimal impact on SIZ degradation. In contrast, Ca^{2+}, HCO_3^-, and DOM significantly inhibited the degradation efficiency. Ca^{2+} could have formed small amounts of $(Ca(SIZ)_X{\cdot}nH_2O)$ metal complexes, which deposited on the catalyst surface, occupying active sites and hindering degradation efficiency.[55] The negative impact of HCO_3^{2-} was likely due to these anions potentially consuming a significant amount of light-excited h^+ and •OH radicals.[58] Furthermore, dissolved organic matter (DOM) in water significantly inhibited its photocatalytic activity by scavenging •OH and $O_2^{\bullet -}$ radicals and obstructing the catalyst's light absorption.[42]

Moreover, the initial pH in water bodies is recognized as a crucial factor influencing degradation rates. As depicted in Figure 8b, as the pH of water bodies increased from 3 to 11, the degradation efficiency of SIZ gradually declined. The zero-point potential of 3S-BOB was measured to be approximately 5.1 by using instrumentation. Literature review indicated dissociation constants of SIZ as pK_a = 1.5 and 5.0.[59] This suggested that when the pH ranged from 1.5 to 5.0, SIZ remained in a neutral mode, facilitating adsorption on charged substances and thereby promoting photocatalysis. However, when the pH exceeded 5.0, SIZ dissociated into an anionic mode. At this stage, the material surface acquired a negative charge, causing electrostatic repulsion. As the pH continued to rise, this repulsion grew stronger, consequently hindering the photocatalytic performance.

As shown in Figure 8c, we investigated the effect of different catalyst dosages on the SIZ degradation. The degradation efficiency significantly increased as the catalyst dosage increased from 0.1 to 0.8 mg L^{-1}. However, the rate of increase was not substantial when the catalyst dosage was increased from 0.8 to 1.2 mg L^{-1}. It could be speculated that the higher concentration of catalyst at high dosages increased

https://doi.org/10.1021/acs.langmuir.5c06805
Langmuir 2026, 42, 8006−8017

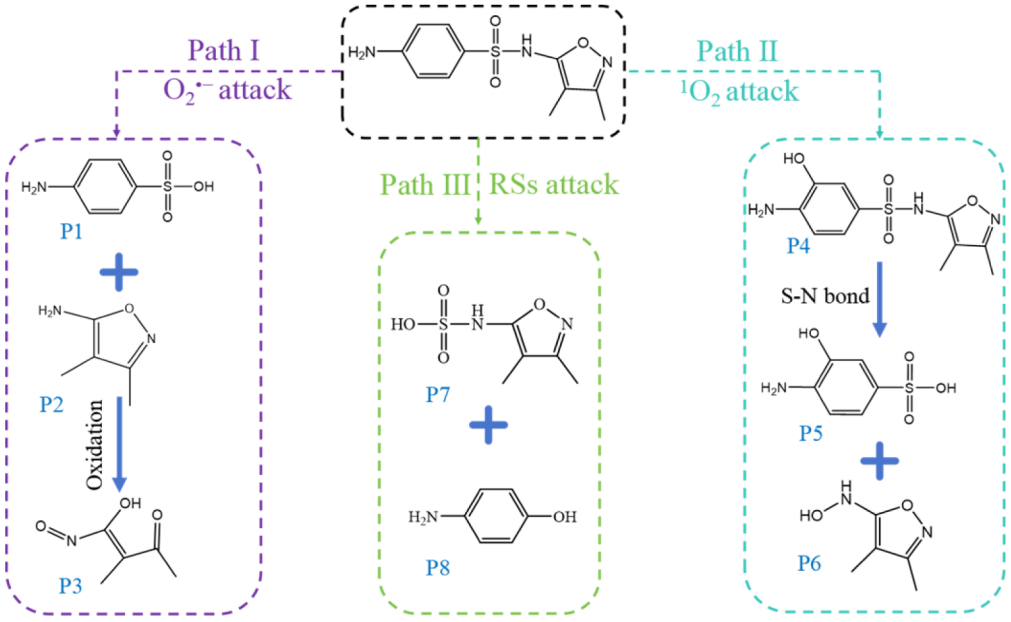

Figure 9. Proposed transformation pathways of the SIZ.

the turbidity of the solution, thereby affecting the transmission of light through water.

To assess the potential applicability of 3S-BOB, the impact of varying initial pollutant concentrations on the SIZ degradation by the material was studied. As shown in Figure 8d, the degradation efficiency of 3S-BOB slightly decreased with increasing pollutant concentration in the range of 5−25 mg L^{-1}. However, at a pollutant concentration of 25 mg L^{-1}, the degradation rate remained above 95%, indicating that 3S-BOB maintained a high removal efficiency of SIZ over a wide range of pollutant concentrations. In conclusion, the 3S-BOB photocatalytic system demonstrated an excellent performance under various environmental conditions.

Degradation Pathway of SIZ

The degradation products were further studied using HRAM LC-MS/MS (Text S8), identifying 8 intermediate products (Table S3 and Figure S8) and deriving three degradation pathways (Figure 9). In pathway I, the S−N bond linking the benzene and triazole moieties was attacked by $O_2^{\bullet-}$, leading to the formation of P1 ($+m/z$ = 284.3307) and P2 ($+m/z$ = 284.3307), which were subsequently oxidized by reactive species to form P3.[29] In pathway II, the benzene ring of SIZ was prone to electrophilic attack by $^1O_2$, coupled with the synergistic effect of phenylamine hydroxylation, leading to the formation of P4 ($+m/z$ = 284.3307). Subsequently, the S−N bond of P4 was cleaved to form P5 ($+m/z$ = 190.0185), which ultimately underwent hydroxylation-dehydrogenation on the pentagon to convert to P6 ($+m/z$ = 127.0502).[60] In pathway III, the S−C bond in the pollutant was attacked by •OH, h^+, and $O_2^{\bullet-}$, leading to cleavage and the formation of byproducts P7 (m/z = 193.0278) and P8 (m/z = 193.0278).[58]

To further investigate the mineralization capability of 3S-BOB for SIZ under irradiation, we obtained the total organic carbon (TOC) degradation curve (Text S11). According to Figure S9, the TOC content gradually decreased to 55% after 1.5 h of irradiation. These results indicated that the 3S-BOB photocatalytic system effectively degraded SIZ and ultimately mineralized it into water and carbon dioxide.

CONCLUSION

In summary, we successfully synthesized sulfur-doped BiOBr via a simple one-step hydrothermal method. Incorporating sulfur not only expanded the specific surface area, providing additional catalytic sites for enhanced adsorption of O_2 and organic pollutants, but also induced the formation of numerous oxygen vacancies, significantly enhancing the material's ability to activate molecular oxygen. Furthermore, the strengthened built-in electric field (BIEF) in 3S-BOB provided ample driving force for the dissociation of excitons, accelerating the separation and migration of carriers and thereby increasing the electron concentration by 1.45 times. Consequently, in photocatalytic degradation experiments, the photocatalytic activity of 3S-BOB was increased 8.07-fold compared to that of BiOBr. Quenching experiments and ESR techniques identified the main active species in the 3S-BOB system as $O_2^{\bullet-}$, h^+, and $^1O_2$. We proposed three possible degradation pathways based on the identification of intermediate products. This study proposes a strategy to enhance photocatalytic activity by adjusting the BIEF and manipulating excitonic effects, offering valuable insights for the rational design of high-performance photocatalysts through doping engineering.

ASSOCIATED CONTENT

Supporting Information

The Supporting Information is available free of charge at https://pubs.acs.org/doi/10.1021/acs.langmuir.5c06805.

Chemical reagents (Text S1); characterization (Text S2); antibiotic detection parameters by liquid chromatography (Text S3); computational details (Text S4); calculation of built-in electric field strength (Text S5); calculation of photoluminescence technology (Text S6); calculation of carrier density (Text S7); identification of photocatalytic transformation products (Text S8); determination of reactive species (Text S9); measurements of $O_2^{\bullet-}$ (Text S10); TOC measurement (Text S11); HPLC analytical parameters for SIZ (Table S1); the actual sulfur content in different prepared samples

https://doi.org/10.1021/acs.langmuir.5c06805
Langmuir 2026, 42, 8006−8017

(Table S2); transformation products from the photocatalytic degradation of SIZ (Table S3); schematic diagram of the photocatalytic reaction setup (Figure S1); XPS spectra (Figure S2); the geometric structural model of 3S-BOB (Figure S3); the adsorption capacity of the samples to SIZ in the dark (Figure S4); photodegradation of SIZ using 3S-BOB in cycling run (Figure S5); UV-vis absorbance spectra (Figure S6); effect of initial pH on the adsorption capacity of 3S-BOB for SIZ in the dark (Figure S7); mass spectrum of the intermediate products (Figure S8); TOC removal rate during the degradation of SIZ by 3S-BOB (Figure S9) (PDF)

AUTHOR INFORMATION

Corresponding Authors

Daguang Li − *College of Light Chemical Industry and Materials Engineering, Shunde Polytechnic University, Foshan 528333, China*; orcid.org/0009-0001-5275-9727; Email: ldguang918@163.com

Wenying Lv − *Guangdong Key Laboratory of Environmental Catalysis and Health Risk Control, School of Environmental Science and Engineering, Institute of Environmental Health and Pollution Control, Guangdong University of Technology, Guangzhou 510006, China*; Email: lvwy612@163.com

Authors

Lingzhi Shen − *Guangdong Key Laboratory of Environmental Catalysis and Health Risk Control, School of Environmental Science and Engineering, Institute of Environmental Health and Pollution Control, Guangdong University of Technology, Guangzhou 510006, China*

Zhenchao Li − *Guangdong Key Laboratory of Environmental Catalysis and Health Risk Control, School of Environmental Science and Engineering, Institute of Environmental Health and Pollution Control, Guangdong University of Technology, Guangzhou 510006, China*

Chenghui Wen − *Guangdong Key Laboratory of Environmental Catalysis and Health Risk Control, School of Environmental Science and Engineering, Institute of Environmental Health and Pollution Control, Guangdong University of Technology, Guangzhou 510006, China*

Zheng Fang − *State Key Laboratory of Biogeology and Environmental Geology, China University of Geosciences, Wuhan 430078, PR China*

Zili Lin − *School of Oceanography, Shanwei Institute of Technology, Shanwei 516600, China*

Wenjun Li − *Guangdong Key Laboratory of Environmental Catalysis and Health Risk Control, School of Environmental Science and Engineering, Institute of Environmental Health and Pollution Control, Guangdong University of Technology, Guangzhou 510006, China*

Jiaxing Huang − *School of Environmental Science and Engineering, Guangdong University of Petrochemical Technology, Maoming 525000, China*

Ningyu Tu − *School of Environmental Science and Engineering, Guangdong University of Petrochemical Technology, Maoming 525000, China*

Guoguang Liu − *Guangdong Key Laboratory of Environmental Catalysis and Health Risk Control, School of Environmental Science and Engineering, Institute of Environmental Health and Pollution Control, Guangdong University of Technology, Guangzhou 510006, China*; orcid.org/0000-0002-1891-6602

Complete contact information is available at: https://pubs.acs.org/10.1021/acs.langmuir.5c06805

Author Contributions

L.S.: Investigation, Validation, Formal analysis, Writing—Original draft; Z.L.: Conceptualization, Data curation, Investigation, Writing—Original draft; D.L.: Methodology, Formal analysis, Writing—Review and editing; C.W.: Methodology, Validation, Writing—Review and editing; Z.F.: Investigation, Supervision; Z.L.: Methodology, Validation; W.L.: Investigation, Formal analysis; J.H.: Resources, Funding acquisition; N.T.: Software, Resources; W.L.: Conceptualization, Supervision, Funding acquisition; G.L.: Resources, Project administration, Funding acquisition. L.S. and Z.L. contributed equally to this work.

Notes

The authors declare no competing financial interest.

ACKNOWLEDGMENTS

This work was supported by the National Natural Science Foundation of China (grant numbers 22076029 and 22176042), the Guangdong Basic and Applied Basic Research Foundation (2023A1515010056), and the Guangdong Provincial Program for Young Innovative Talents in General Higher Education Institutions (2024KQNCX169).

REFERENCES

(1) Wen, C.; Li, D.; Zhong, J.; Wang, Z.; Huang, S.; Liu, H.; Wu, J.; Chen, P.; Lv, W.; Liu, G. In situ synthesis of S-scheme AgBr/BiOBr for efficient degradation of sulfonamide antibiotics: Synergistic effects of oxygen vacancies and heterojunctions promote exciton dissociation. *Chem. Eng. J* **2022**, *450*, 138075.

(2) Xiao, J.; Li, Y.; Dong, H.; Pang, Z.; Zhao, M.; Huang, D.; Dong, J.; Li, L. Highly efficient activation of peracetic acid via zero-valent iron-copper bimetallic nanoparticles (nZVIC) for the oxidation of sulfamethazine in aqueous solution under neutral condition. *Appl. Catal., B* **2024**, *340*, 123183.

(3) Ni, J.; Wen, Y.; Pan, D.; Bai, J.; Zhou, B.; Zhao, S.; Wang, Z.; Liu, Y.; Zeng, Q. Light-driven simultaneous water purification and green energy production by photocatalytic fuel cell: A comprehensive review on current status, challenges, and perspectives. *Chem. Eng. J* **2023**, *473*, 145162.

(4) Lin, Z.; Wang, Z.; Xu, Z.; Xiao, Z.; Fang, Z.; Luo, J.; Li, P.; Chen, P.; Lv, W.; Liu, G. Self-assembly construction of 1D carbon nitride nanotubes and cobalt-modified for superior photocatalytic degradation of sulfonamide antibiotics. *Chemosphere* **2023**, *343*, 140299.

(5) Li, D.; Zhang, G.; Li, W.; Fang, Z.; Liu, H.; Lv, W.; Liu, G. Magnetic nitrogen-doped carbon nanotubes as activators of peroxymonosulfate and their application in non-radical degradation of sulfonamide antibiotics. *J. Clean. Prod* **2022**, *380*, 135064.

(6) He, Z.; Chen, M.; Xu, M.; Zhou, Y.; Zhang, Y.; Hu, G. $LaCo_{0.5}Ni_{0.5}O_3$ perovskite for efficient sulfafurazole degradation via peroxymonosulfate activation: Catalytic mechanism of interfacial structure. *Appl. Catal., B* **2023**, *335*, 122883.

(7) Jiang, Z.-R.; Wang, P.; Zhou, Y.-X.; Wang, C.; Jiang, J.; Lan, Y.; Chen, C. Fabrication of a 3D-blocky catalyst (CoMnOx@sponge) via mooring Co-Mn bimetallic oxide on sponge to activate peroxymonosulfate for convenient and efficient degradation of sulfonamide antibiotics. *Chem. Eng. J* **2022**, *446*, 137306.

(8) Luo, K.; Shi, Y.; Huang, R.; Wei, X.; Wu, Z.; Zhou, P.; Zhang, H.; Wang, Y.; Xiong, Z.; Lai, B. Activation of periodate by N-doped iron-based porous carbon for degradation of sulfisoxazole: Signifi-

cance of catalyst-mediated electron transfer mechanism. *J. Hazard. Mater* **2023**, *457*, 131790.
(9) Dai, X.; Liu, Z.; Li, H.; Zhang, K.; Wang, H.; Ma, D.; Chen, W. Efficient photocatalytic activity by constructing double anion defects: synergistic and process mechanism. *Appl. Catal., B* **2024**, *357*, 124293.
(10) Huang, S.; Wang, Y.; Wan, J.; Yan, Z.; Ma, Y.; Zhang, G.; Wang, S. Ti_3C_2Tx as electron-hole transfer mediators to enhance AgBr/BiOBr Z heterojunction photocatalytic for the degradation of Tetrabromobisphenol A: Mechanism Insight. *Appl. Catal., B* **2022**, *319*, 121913.
(11) Zhong, S.; Wang, Y.; Chen, Y.; Jiang, X.; Lin, M.; Lin, C.; Lin, T.; Gao, M.; Zhao, C.; Wu, X. Improved piezo-photocatalysis for aquatic multi-pollutant removal via BiOBr/$BaTiO_3$ heterojunction construction. *Chem. Eng. J* **2024**, *488*, 151002.
(12) Lu, L.; Zhang, H.; Sun, Z.; Wang, J.; Wang, H.; Xue, J.; Shen, Q.; Li, Q. Creation of robust oxygen vacancies in 2D ultrathin BiOBr nanosheets by irradiation through photocatalytic memory effect for enhanced CO_2 reduction. *Chem. Eng. J* **2023**, *477*, 146892.
(13) Zhou, R.; Zhang, D.; Wang, P.; Huang, Y. Regulation of excitons dissociation in AgI/Bi_3O_4Br for advanced reactive oxygen species generation towards photodegradation. *Appl. Catal., B* **2021**, *285*, 119820.
(14) Wang, H.; Chen, S.; Yong, D.; Zhang, X.; Li, S.; Shao, W.; Sun, X.; Pan, B.; Xie, Y. Giant Electron−Hole Interactions in Confined Layered Structures for Molecular Oxygen Activation. *J. Am. Chem. Soc* **2017**, *139* (13), 4737−4742.
(15) Li, D.; Liu, Y.; Wen, C.; Huang, J.; Li, R.; Liu, H.; Zhong, J.; Chen, P.; Lv, W.; Liu, G. Construction of dual transfer channels in graphitic carbon nitride photocatalyst for high-efficiency environmental pollution remediation: Enhanced exciton dissociation and carrier migration. *J. Hazard. Mater* **2022**, *436*, 129171.
(16) Zhang, W. J.; Deng, Z. Z.; Deng, J. Y.; Au, C. T.; Liao, Y. F.; Yang, H.; Liu, Q. Q. Regulating the exciton binding energy of covalent triazine frameworks for enhancing photocatalysis. *J. Mater. Chem. A* **2022**, *10* (42), 22419−22427.
(17) Qian, Y.; Li, D.; Han, Y.; Jiang, H.-L. Photocatalytic Molecular Oxygen Activation by Regulating Excitonic Effects in Covalent Organic Frameworks. *J. Am. Chem. Soc* **2020**, *142* (49), 20763−20771.
(18) Li, F.; Yue, X.; Zhang, D.; Fan, J.; Xiang, Q. Targeted regulation of exciton dissociation in graphitic carbon nitride by vacancy modification for efficient photocatalytic CO_2 reduction. *Appl. Catal., B* **2021**, *292*, 120179.
(19) Tao, Y.; Ma, Z.; Wang, W.; Zhang, C.; Fu, L.; Zhu, Q.; Li, Y.; Li, G.; Zhang, D. Nickel Phosphide Clusters Sensitized TiO_2 Nanotube Arrays as Highly Efficient Photoanode for Photoelectrocatalytic Urea Oxidation. *Adv. Funct. Mater* **2023**, *33* (9), 2211169.
(20) Shi, Y.; Yang, Z.; Shi, L.; Li, H.; Liu, X.; Zhang, X.; Cheng, J.; Liang, C.; Cao, S.; Guo, F.; Liu, X.; Ai, Z.; Zhang, L. Surface Boronizing Can Weaken the Excitonic Effects of BiOBr Nanosheets for Efficient O_2 Activation and Selective NO Oxidation under Visible Light Irradiation. *Environ. Sci. Technol* **2022**, *56* (20), 14478−14486.
(21) Wang, H.; Yong, D. Y.; Chen, S. C.; Jiang, S. L.; Zhang, X. D.; Shao, W.; Zhang, Q.; Yan, W. S.; Pan, B. C.; Xie, Y. Oxygen-Vacancy-Mediated Exciton Dissociation in BiOBr for Boosting Charge-Carrier-Involved Molecular Oxygen Activation (vol 140, pg 1760, 2018). *J. Am. Chem. Soc* **2018**, *140* (15), 5320−5320.
(22) Wu, J.; Tao, Y.; Zhang, C.; Zhu, Q.; Zhang, D.; Li, G. Activation of chloride by oxygen vacancies-enriched TiO_2 photoanode for efficient photoelectrochemical treatment of persistent organic pollutants and simultaneous H_2 generation. *J. Hazard. Mater* **2023**, *443*, 130363.
(23) Zhang, C.; Deng, Y.; Wan, Q.; Zeng, H.; Wang, H.; Yu, H.; Pang, H.; Zhang, W.; Yuan, X.; Huang, J. Built-in electric field boosted exciton dissociation in sulfur doped BiOCl with abundant oxygen vacancies for transforming the pathway of molecular oxygen activation. *Appl. Catal., B* **2024**, *343*, 123557.
(24) Liu, J.; Kang, S.; Wu, X.; Pan, Y.; Yan, Y.; Liu, C.; Wang, C.; Jia, H.; Shi, M.; Tong, G. Advanced hierarchical porous carbon nanosheets: Controlled synthesis, optimization strategy, environmental application and regeneration utilization. *J. Environ. Chem. Eng* **2025**, *13* (6), 120514.
(25) Shi, M.; Jia, H.; Liu, J.; Gao, M.; Wang, C.; Wang, F.; Xia, M.; Jin, W.; Tong, G. Engineering sustainable porous carbon electrodes for practical-level capacitive deionization desalination. *Coord. Chem. Rev* **2025**, *543*, 216949.
(26) Dai, W.-W.; Zhao, Z.-Y. Defect Physics of BiOI as High Efficient Photocatalyst Driven by Visible Light. *J. Am. Ceram. Soc* **2016**, *99* (9), 3015−3024.
(27) Li, J.; Zhang, L.; Li, Y.; Yu, Y. Synthesis and internal electric field dependent photoreactivity of Bi_3O_4Cl single-crystalline nanosheets with high {001} facet exposure percentages. *Nanoscale* **2014**, *6* (1), 167−171.
(28) Jin, Y.; Li, F.; Li, T.; Xing, X. C.; Fan, W. H.; Zhang, L. L.; Hu, C. Enhanced internal electric field in S-doped BiOBr for intercalation, adsorption and degradation of ciprofloxacin by photoinitiation. *Appl. Catal., B* **2022**, *302*, 120824.
(29) Tan, C.; Zhang, Q.; Zheng, X.; Liu, H.; Chen, P.; Zhang, W.; Liu, Y.; Lv, W.; Liu, G. Photocatalytic degradation of sulfonamides in 4-phenoxyphenol-modified g-C_3N_4 composites: Performance and mechanism. *Chem. Eng. J* **2021**, *421*, 127864.
(30) Geioushy, R. A.; El-Sheikh, S. M.; Azzam, A. B.; Salah, B. A.; El-Dars, F. M. One-pot fabrication of $BiPO_4/Bi_2S_3$ hybrid structures for visible-light driven reduction of hazardous Cr(VI). *J. Hazard. Mater* **2020**, *381*, 120955.
(31) Yang, L.; Hu, Y.; Zhang, L. Architecting Z-scheme Bi_2S_3@CoO with 3D chrysanthemums-like architecture for both photoeletro-oxidization and -reduction performance under visible light. *Chem. Eng. J* **2019**, *378*, 122092.
(32) Li, W.; Zou, Y.; Geng, X.; Xiao, F.; An, G.; Wang, D. Constructing highly catalytic oxidation over BiOBr-based hierarchical microspheres: Importance of redox potential of doped cations. *Mol. Catal* **2017**, *438*, 19−29.
(33) Liu, X.; Yang, Y.; Li, H.; Yang, Z.; Fang, Y. Visible light degradation of tetracycline using oxygen-rich titanium dioxide nanosheets decorated by carbon quantum dots. *Chem. Eng. J* **2021**, *408*, 127259.
(34) Shi, Y.; Xiong, X.; Ding, S.; Liu, X.; Jiang, Q.; Hu, J. In-situ topotactic synthesis and photocatalytic activity of plate-like BiOCl/2D networks Bi_2S_3 heterostructures. *Appl. Catal., B* **2018**, *220*, 570−580.
(35) Yang, B.; He, L.; Guo, Y.; Zhao, T.; Shi, Z.; Liu, C.; Yang, M.; Yang, Q.; Sun, S.; Cui, J. Enhanced catalysis for degradation of antibiotic by hydroxyl-functionalized S-doped BiOCl with high capacity of local spatial charge separation. *Colloids Surf., A* **2023**, *669*, 131448.
(36) Yang, X.; Sun, S.; Ye, L.; Yun, D.; Liu, C.; Guo, Y.; Yang, B.; Yang, M.; Yang, Q.; Liang, S.; Cui, J. One-pot integration of S-doped BiOCl and ZnO into type-II photocatalysts: Simultaneously boosting bulk and surface charge separation for enhanced antibiotic removal. *Sep. Purif. Technol* **2022**, *299*, 121725.
(37) Zhang, W.; Bian, Z.; Peng, Y.; Tang, H.; Wang, H. Dual-function oxygen vacancy of BiOBr intensifies pollutant adsorption and molecular oxygen activation to remove tetracycline hydrochloride. *Chem. Eng. J* **2023**, *451*, 138731.
(38) Ma, J.; Xu, L.; Yin, Z.; Li, Z.; Dong, X.; Song, Z.; Chen, D.; Hu, R.; Wang, Q.; Han, J.; Yang, Z.; Qiu, J.; Li, Y. "One stone four birds" design atom co-sharing BiOBr/Bi_2S_3 S-scheme heterojunction photothermal synergistic enhanced full-spectrum photocatalytic activity. *Appl. Catal., B* **2024**, *344*, 123601.
(39) Gu, Y.; Li, Y.; Feng, H.; Han, Y.; Li, Z. Built-in electric field induced S-scheme g-C_3N_4 homojunction for efficient photocatalytic hydrogen evolution: Interfacial engineering and morphology control. *Nano Res* **2024**, *17* (6), 4961−4970.
(40) Jia, X. M.; Hu, C.; Sun, H. Y.; Cao, J.; Lin, H. L.; Li, X. Y.; Chen, S. F. A dual defect co-modified S-scheme heterojunction for

https://doi.org/10.1021/acs.langmuir.5c06805
Langmuir 2026, 42, 8006−8017

boosting photocatalytic CO_2 reduction coupled with tetracycline oxidation. *Appl. Catal., B* **2023**, *324*, 122232.
(41) Zhang, G.; Li, D.; Liu, M.; Wang, Y.; Zhang, J.; Zhang, Y.; Liu, H.; Li, W.; Li, Z.; Lv, W.; Liu, G. Non-noble plasmonic TiN modified BiOBr for the piezo-photocatalytic removal of sulfisoxazole: Simultaneous improvement of photocatalytic and piezoelectric properties. *Sep. Purif. Technol* **2024**, *337*, 126358.
(42) Liu, M.; Chen, Y.; Li, D.; Huang, S.; Fang, Z.; Xiao, Z.; Liu, H.; Chen, P.; Lv, W.; Liu, G. Visible-light-driven BNQD/$BiVO_4$ material with enhanced photocatalytic activities for naproxen degradation and kinetic insights. *Environ. Sci.: Nano* **2023**, *10* (8), 2022−2034.
(43) Jing, J.; Yang, J.; Zhang, Z.; Zhu, Y. Supramolecular Zinc Porphyrin Photocatalyst with Strong Reduction Ability and Robust Built-In Electric Field for Highly Efficient Hydrogen Production. *Adv. Energy Mater* **2021**, *11* (29), 2101392.
(44) Li, J.; Zhan, G.; Yu, Y.; Zhang, L. Superior visible light hydrogen evolution of Janus bilayer junctions via atomic-level charge flow steering. *Nat. Commun* **2016**, *7*, 11480.
(45) Li, J.; Cai, L.; Shang, J.; Yu, Y.; Zhang, L. Giant Enhancement of Internal Electric Field Boosting Bulk Charge Separation for Photocatalysis. *Adv. Mater* **2016**, *28* (21), 4059−4064.
(46) Li, Z.; Wen, C.; Li, D.; Fang, Z.; Lin, Z.; Liu, D.; Wang, Y.; Zhang, X.; Chen, P.; Lv, W.; Liu, G. Insights into nitrogen-doped BiOBr with oxygen vacancy and carbon quantum dots photocatalysts for the degradation of sulfonamide antibiotics: Actions to promote exciton dissociation and carrier migration. *Chem. Eng. J* **2024**, *492*, 152449.
(47) Kanata, T.; Matsunaga, M.; Takakura, H.; Hamakawa, Y.; Nishino, T.Photoreflectance characterization of built-in potential in MBE produced as-grown GaAs surface*Modulation Spectroscopy*-SPIE1990*128656*−65
(48) Wang, K.; Cheng, M.; Xia, F.; Cao, N.; Zhang, F.; Ni, W.; Yue, X.; Yan, K.; He, Y.; Shi, Y.; Dai, W.; Xie, P. Atomically Dispersed Electron Traps in Cu Doped BiOBr Boosting CO_2 Reduction to Methanol by Pure H2O. *Small* **2023**, *19* (14), 2207581.
(49) Wang, H.; Sun, X.; Li, D.; Zhang, X.; Chen, S.; Shao, W.; Tian, Y.; Xie, Y. Boosting Hot-Electron Generation: Exciton Dissociation at the Order−Disorder Interfaces in Polymeric Photocatalysts. *J. Am. Chem. Soc* **2017**, *139* (6), 2468−2473.
(50) Shi, Y.; Zhan, G.; Li, H.; Wang, X.; Liu, X.; Shi, L.; Wei, K.; Ling, C.; Li, Z.; Wang, H.; et al. Simultaneous Manipulation of Bulk Excitons and Surface Defects for Ultrastable and Highly Selective CO_2 Photoreduction. *Adv. Mater* **2021**, *33* (38), 2100143.
(51) Zhang, M. M.; Lai, C.; Li, B. S.; Xu, F. H.; Huang, D. L.; Liu, S. Y.; Qin, L.; Fu, Y. K.; Liu, X. G.; Yi, H.; Zhang, Y. J.; He, J. F.; Chen, L. Unravelling the role of dual quantum dots cocatalyst in 0D/2D heterojunction photocatalyst for promoting photocatalytic organic pollutant degradation. *Chem. Eng. J* **2020**, *396*, 125343.
(52) Monny, S. A.; Wang, Z. L.; Lin, T.; Chen, P.; Luo, B.; Wang, L. Z. Designing efficient $Bi_2Fe_4O_9$ photoanodes bulk and surface defect engineering. *Chem. Commun* **2020**, *56* (65), 9376−9379.
(53) Guo, H.; Niu, C.-G.; Liang, C.; Niu, H.-Y.; Yang, Y.-Y.; Liu, H.-Y.; Tang, N.; Fang, H.-X. Highly crystalline porous carbon nitride with electron accumulation capacity: Promoting exciton dissociation and charge carrier generation for photocatalytic molecular oxygen activation. *Chem. Eng. J* **2021**, *409*, 128030.
(54) Yu, H.; Huang, J.; Jiang, L.; Yuan, X.; Yi, K.; Zhang, W.; Zhang, J.; Chen, H. Steering photo-excitons towards active sites: Intensified substrates affinity and spatial charge separation for photocatalytic molecular oxygen activation and pollutant removal. *Chem. Eng. J* **2021**, *408*, 127334.
(55) Liu, K.; Wang, L.; Fu, T.; Zhang, H.; Lu, C.; Tong, Z.; Yang, Y.; Peng, Y. Oxygen-functionalized Ti_3C_2 MXene/exfoliated montmorillonite supported S-scheme BiOBr/Bi_2MoO_6 heterostructures for efficient photocatalytic quinolone antibiotics degradation. *Chem. Eng. J* **2023**, *457*, 141271.
(56) Lin, Z.; Wu, Y.; Jin, X.; Liang, D.; Jin, Y.; Huang, S.; Wang, Z.; Liu, H.; Chen, P.; Lv, W.; Liu, G. Facile synthesis of direct Z-scheme UiO-66-NH_2/PhC_2Cu heterojunction with ultrahigh redox potential for enhanced photocatalytic Cr(VI) reduction and NOR degradation. *J. Hazard. Mater* **2023**, *443*, 130195.
(57) Chen, Y.; Lin, Z.; Zhang, J.; Liu, Y.; Liang, D.; Li, D.; Zhang, Y.; Liu, H.; Chen, P.; Lv, W.; Liu, G. Strategy for improvement of molecular oxygen activation capacity of PPECu by chlorine doping for water decontamination. *J. Hazard. Mater* **2023**, *460*, 132421.
(58) Zhong, J.; Huang, J.; Liu, Y.; Li, D.; Tan, C.; Chen, P.; Liu, H.; Zheng, X.; Wen, C.; Lv, W.; Liu, G. Construction of double-functionalized g-C_3N_4 heterojunction structure via optimized charge transfer for the synergistically enhanced photocatalytic degradation of sulfonamides and H_2O_2 production. *J. Hazard. Mater* **2022**, *422*, 126868.
(59) Zhang, Y.; Chen, P.; Lv, W.; Xiao, Z.; Zhang, J.; Wu, J.; Lin, Z.; Zhang, G.; Yu, Z.; Liu, H.; Liu, G. Key role of Fe(VI)-activated Bi_2WO_6 in the photocatalytic oxidation of sulfonamides: Mediated electron transfer mechanism. *J. Hazard. Mater* **2023**, *458*, 132009.
(60) Yu, Z.; Wu, J.; Zhang, J.; Chen, X.; Wang, Z.; Zhang, Y.; Li, D.; Chen, J.; Liu, H.; Chen, P.; Lv, W.; Liu, G. Carbon nitride nanotubes anchored with Cu(I) triggers peracetic acid activation with visible light for removal of antibiotic contaminants: Probing mechanisms of non-radical pathways and identifying active sites. *J. Hazard. Mater* **2023**, *460*, 132401.

https://doi.org/10.1021/acs.langmuir.5c06805
Langmuir 2026, 42, 8006−8017